THE ASTROPHYSICAL JOURNAL, 367:333–349, 1991 January 20

RADIATIVE TRANSFER IN ASTRONOMICAL MASERS. III. FILAMENTARY MASERS

MOSHE ELITZUR
Department of Physics and Astronomy, University of Kentucky, Lexington, KY 40506
CHRISTOPHER F. MCKEE
Astronomy Department, University of California, Berkeley, CA 94720
AND
DAVID J. HOLLENBACH
NASA Ames Research Center, MS 245-6, Moffett Field, CA 94035
Received 1989 December 26; accepted 1990 July 20

ABSTRACT

This paper, the last in a series, presents the complete solution of a filamentary maser. The contribution of rays emanating from the filament sidewall is essential for the solution self-consistency during saturation. We develop an integral equation to calculate this contribution, devise an iteration scheme to solve it, and perform the first two iterations. The solution provides complete expressions for the distributions of intensity and flux across the source as functions of position and direction with regard to the axis. One consequence of radiation beaming, somewhat surprising at first, is that the filament appears *smaller* when viewed off-axis, at angles exceeding the cap's opening angle. From the detailed results we devise the number distribution of brightness temperatures in a large sample of randomly oriented filaments with an arbitrary distribution of lengths. A thorough comparison of the filamentary and spherical geometries is presented with possible observational tests to differentiate between the two.

The effects of external radiation on the maser structure and intensity are also studied. Explicit expressions for the brightness and flux in this situation are provided, including detailed analysis of two interacting filaments and a foreground slab amplifying a background filament. We propose that the two giant bursts of H_2O maser emission observed in W49 and Orion were the result of such interactions. Rapid time variations reported for the Orion burst may best be explained with amplification of a background maser filament by a foreground maser slab, initially unsaturated.

Subject headings: masers — radiative transfer

I. INTRODUCTION

The filamentary geometry is of particular importance to theory of astronomical masers, since strong interstellar masers are most likely elongated tubes, or filaments (e.g., Genzel 1986). In all likelihood, the filamentary structures arise from the requirement of velocity coherence rather than density contrast. We have recently constructed a comprehensive model for H_2O masers in star-forming regions where the filamentary geometry is an integral part of the model (Elitzur, Hollenbach and McKee 1989, hereafter EHM). Important ingredients in such a model, and any other of that nature, are the expressions for the beaming angle of the radiation, the intensity as a function of angle from the beam axis, and the exact relations between the pump rate and the expected brightness temperature and luminosity at any angle to the filament axis.

In spite of its great significance, the only investigation pertaining to the general theory of filamentary masers is the work of Goldreich and Keeley (1972), where the cylindrical maser was studied in what they described as a "very rough way." The aim of this paper is to correct this situation by presenting the complete solution of a filamentary maser. The solution is constructed utilizing the framework developed in the previous two papers of this series, which present the detailed solutions for a linear maser (Elitzur 1990*a*, hereafter Paper I) and a three-dimensional maser of an arbitrary shape (Elitzur 1990*b*, hereafter Paper II).[1] This general solution is applicable to any geometry, different configurations requiring only the specific dependence of the beaming angle on the distance traveled along the ray path. Here we employ these methods in the filamentary geometry.

Because of the particular relevance of the filamentary geometry to astronomical masers, this paper can be considered the culmination of the series. Although frequent reference is made to the two previous papers, the presentation here is essentially self-contained. In § II we present the solution of an unsaturated filament. This enables us to define precisely the conditions under which the maser can be considered "filamentary." The solution of a saturated maser without background radiation is worked out in detail in § III. Because of the contribution of rays emanating from the filament sidewall, a complete solution of this problem requires a self-consistency approach that results in an integral equation. The concepts leading to this equation are well illustrated by the first iteration solution, which lends itself to simple physical interpretation and provides the correct behavior of the complete solution. In order to keep the presentation more tractable we confine the body of the manuscript to the first iteration; the discussion of the full problem and the solution of the next iteration are deferred to Appendix A. The effect of background radiation on the structure and intensity of a filamentary maser is discussed in § IV. In a recent paper, Deguchi and Watson (1989) suggested that very bright H_2O masers in star-forming regions are the result of the interaction of two maser filaments. We develop accurate expressions for the brightness temperature and luminosity of such a maser model, as well as

[1] Notations follow those of the previous papers. Equations from Papers I and II are referenced with I and II, respectively, followed by the equation number in the appropriate paper.

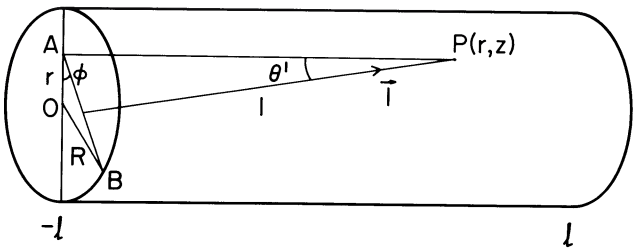

FIG. 1.—Geometric notations and rays in cylindrical masers

other configurations, and suggest that it accounts for the two unusual giant bursts of H_2O maser emission observed in Orion and in W49 (Matveenko 1986). In § V we discuss the observational implications of our results, including a thorough comparison with the spherical geometry. The results with most direct relevance to observations are collected in § VI for handy reference.

II. UNSATURATED FILAMENTS

To provide a precise definition for the term "filament" we start with the prototype, an elongated cylinder (Fig. 1). As in the linear case (Paper I), positions along the cylinder are specified by z, which again varies in the interval $[-\ell, \ell]$. The cylinder radius is R and its aspect ratio, length over width, is

$$a = \ell/R \,. \tag{2.1}$$

We consider only sources where $a \gg 1$. When this condition is met, the geometrical shape of the cross section becomes irrelevant. If the cross section area is A, we define an effective radius according to

$$R = (A/\pi)^{1/2} \tag{2.2}$$

and an aspect ratio according to equation (1). A "filament" is an arbitrary elongated structure with a constant cross section and $a \gg 1$; an additional constraint that further restricts the definition is given below. A long cylinder is simply a filament with a circular cross section. Even the assumption of a constant cross section can be relaxed, provided the shape variations are moderate, but this will not be done here. Other quantities of importance are the cap opening angle ϑ_0 and the corresponding solid angle Ω_0, obtained from

$$\vartheta_0 = R/(2\ell) = 1/(2a) \,,$$
$$\Omega_0 = \pi\vartheta_0^2 = A/(4\ell^2) = \pi/(4a^2) \,. \tag{2.3}$$

Evidently, both ϑ_0 and $\Omega_0/4\pi$ are small parameters ($\ll 1$).

When the maser is unsaturated throughout, the intensity is obtained from equation (I.2.5)

$$I_\nu = (S_0 + I_e) \exp(\kappa_{0\nu} l) - S_0 \,, \tag{2.4}$$

where l is the distance along the ray from its entry point (note that the maximum value of pathlength l is $2\ell/\cos 2\vartheta_0$), S_0 and $\kappa_{0\nu}$ are, respectively, the unsaturated source function and absorption coefficient, and I_e is the intensity of external radiation that may illuminate the maser; this is neglected until § IV. In particular, the expressions for $I_\nu(z, r, \mu = \pm 1)$, the intensity on rays parallel to the axis, are the same as the corresponding $I_{\nu\pm}(z)$ of the unsaturated linear maser (eq. [I.3.3]). The angle-averaged intensity is given by

$$J_\nu = \tfrac{1}{2} \int I_\nu(\vartheta) \sin\vartheta \, d\vartheta \,, \tag{2.5}$$

where ϑ denotes inclination angle from the z-axis and $I_\nu(\vartheta)$ is obtained from equation (2.4) with the appropriate (ϑ-dependent) length traveled through the source. The small-angle approximation is justified in this integration because large values of ϑ correspond to short ray lengths and (exponentially) small intensities, so their contribution to the integral is negligible. Consider the exit point on the main axis ($r = 0, z = \ell$). The integration range can be divided to two parts, separated by ϑ_0—the inclination angle of the longest ray, the one separating the cap from the sidewall (Fig. 1). The integration region $\vartheta \le \vartheta_0$ corresponds to rays that originated from the opposite cap and its contribution to $J_\nu(\ell)$ will be denoted $J_{\nu,\mathrm{cap}}$. The length traveled through the source by such cap rays is $2\ell/\cos\vartheta \simeq 2\ell(1 + \frac{1}{2}\vartheta^2)$, so their intensity obeys

$$\vartheta \le \vartheta_0 : \quad I_\nu(\vartheta) = S_0 \exp[2\kappa_{0\nu}\ell(1 + \tfrac{1}{2}\vartheta^2)] \,. \tag{2.6}$$

The corresponding angular integration is immediate, leading to

$$J_{\nu,\mathrm{cap}} = \frac{1}{4}\vartheta_0^2 S_0 \exp(2\kappa_{0\nu}\ell) \frac{\exp(\kappa_{0\nu}\ell\vartheta_0^2) - 1}{\kappa_{0\nu}\ell\vartheta_0^2} \,. \tag{2.7}$$

Note that the factor $\frac{1}{4}\vartheta_0^2$ is simply $\Omega_0/4\pi$.

The variation of $J_{\nu,\mathrm{cap}}$ with overall length displays a different behavior in two regimes, separated according to the magnitude of $\kappa_{0\nu}\ell\vartheta_0^2$, which is the square of the ratio of two angles: the cap angle ϑ_0 and the angle $\vartheta_r = (\kappa_{0\nu}\ell)^{-1/2}$ that sets the scale for radiation beaming (eq. [II.2.3]). Evidently,

$$\kappa_{0\nu}\ell\vartheta_0^2 = \frac{\vartheta_0^2}{\vartheta_r^2} = \frac{\kappa_{0\nu}R}{4a} \,. \tag{2.8}$$

When $\vartheta_0 > \vartheta_r$, $\kappa_{0\nu}\ell\vartheta_0^2 > 1$ and from equation (2.7),

$$J_{\nu,\mathrm{cap}} = S_0 \frac{\exp[2\kappa_{0\nu}\ell(1 + \frac{1}{2}\vartheta_0^2)]}{4\kappa_{0\nu}\ell} \,. \tag{2.9}$$

This result is similar to the angle-averaged intensity of an unsaturated spherical maser with radius $\ell(1 + \frac{1}{2}\vartheta_0^2)$ (eq. [II.5.5]). Since the radiation pattern is narrower than the cap's opening angle, the intensity of cap rays varies with ϑ and has a dip along the main axis at $\vartheta = 0$ (eq. [2.6]), so the maser cannot really be considered filamentary. The maser can be considered filamentary only when $\vartheta_0 \ll \vartheta_r$, namely $\kappa_{0\nu}\ell\vartheta_0^2 \ll 1$, which leads to

$$J_{\nu,\mathrm{cap}} = (\Omega_0/4\pi) S_0 \exp(2\kappa_{0\nu}\ell) \,, \tag{2.10}$$

as evident from equation [2.7]. This result can also be obtained by assuming that the intensity is constant across the cap, that is,

$$\vartheta \le \vartheta_0 : \quad I_\nu(\vartheta) = I_\nu(0) = S_0 \exp(2\kappa_{0\nu}\ell) \,, \tag{2.11}$$

an approximation justified in this limit. Thus, the filamentary condition requires that not only $\vartheta_0 \ll 1$ (or $a \gg 1$) be obeyed, but also $\vartheta_0 \ll \vartheta_r$ or

$$a \gg \max[1, \kappa_{0\nu}R/4] \,; \tag{2.12}$$

a similar result was derived by Western (1987). This condition ensures that equation (2.11) is obeyed and the intensity variation across the cap can be neglected; it is evident that under these circumstances the shape of the cross section area is irrelevant. As a concrete example we consider our model for H_2O masers in star-forming regions (EHM). A prototype maser feature with $n(H_2) = 10^9$ cm^{-3}, $[H_2O]/[H_2] = 6 \times 10^{-4}$,

$T = 400$ K and $d = 2R = 10^{13}$ cm has $\kappa_{0\nu} R = 3.9$. Therefore, the filamentary condition is obeyed in this case whenever $a \gg 1$.

The other contribution to $J_\nu(z = \ell, r = 0)$ comes from the integration range $\vartheta > \vartheta_0$. This corresponds to rays that originated from the side of the filament (such as the one entering at $-z_i$ in Fig. 1) and can be written as

$$J_{\nu,\text{side}} = \tfrac{1}{2} S_0 \int_{\vartheta_0} \exp(\kappa_{0\nu} R/\vartheta)\vartheta \, d\vartheta \, . \tag{2.13}$$

The upper limit of the integration is irrelevant since the integral is dominated by $\vartheta \simeq \vartheta_0$ due to the rapid decline of the exponential factor at large angles. Utilizing this fact, the integral can be easily performed and the result is

$$J_{\nu,\text{side}} = (\Omega_0/4\pi) S_0 \exp(2\kappa_{0\nu}\ell)/(\kappa_{0\nu}\ell) \, . \tag{2.14}$$

Thus, $J_{\nu,\text{side}} \ll J_{\nu,\text{cap}}$ for unsaturated filaments whenever $\kappa_{0\nu}\ell \gg 1$. It should be noted that the angular integration range of side rays exceeds that of cap rays by a factor of roughly ℓ/R, i.e., the aspect ratio. Nevertheless, their contribution to J_ν is negligible because this increase is more than offset by the exponential decrease of their intensity from that of the cap rays.

This discussion enables us to examine more precisely the applicability of the filamentary model in any given situation. For any elongated structure, the complete solution can always be expanded as a power series in the variable $(\vartheta_0/\vartheta_r)^2 = \kappa_{0\nu} R/4a$. Equation (2.12) ensures that this is a small parameter, and the filamentary solution which we develop here is simply the leading term of this expansion. In this order of approximation, the variation of intensity on planes of constant z can be neglected; that is, $I_\nu = I_\nu(z, \vartheta)$, independent of r. It is easy to show that this also ensures that $J_\nu = J_\nu(z)$, independent of r, thus validating the self-consistency of retaining only the first term of this expansion.

As mentioned above, the filamentary geometry is generated, in all likelihood, by velocity gradients, which determine the geometrical shape of the velocity-coherent region. Inside this region the material is quiescent, since velocity shifts are smaller than the line width, so that further considerations of velocity gradients are irrelevant. One consequence of the filamentary assumption is that the edges are sharp. However, smoothing the filament's edges should make no fundamental difference to the solution, obviously; the relevant property is the relation between the characteristic angles defined by the geometry (ϑ_0) and by the maser radiation pattern (ϑ_r)—the filamentary condition presented in equation (2.12).

III. THE SATURATED MASER

Consider now a succession of models with increasing half-length ℓ and with all the other parameters held fixed. The maser saturates at the length $2\ell_{s\nu}$ when $J_\nu(\ell_{s\nu}) = J_s$, the saturation intensity. This length is now obtained from

$$\left(\frac{R}{2\ell_{s\nu}}\right)^2 \exp(2\kappa_{0\nu}\ell_{s\nu}) = 4\gamma \, , \tag{3.1}$$

where $\gamma = J_s/S_0$. This is again an equation of the form $\exp(x)/x = b$ with $b \gg 1$, and from equation (II.5.7), the saturation length is given by $\kappa_{0\nu}\ell_{s\nu} = \ln(4\gamma^{1/2}/\kappa_{0\nu} R)$, to a good degree of approximation. This relation should be contrasted with the corresponding one for the linear maser, $\kappa_{0\nu}\ell_{s\nu} = \ln(2\gamma)^{1/2}$ (eq. [I.3.5]). Saturation can therefore occur either earlier or later than for a linear maser of the same length, depending on the value of $\kappa_{0\nu} R$.

When its length is further increased, the maser develops a three-zone structure similar to the linear case, with an unsaturated core for $|z| < z_{s\nu}$ and saturated behavior for $|z| > z_{s\nu}$. The core boundary $z_{s\nu}$ is as yet undetermined. The dominant rays carry radiation outward in each saturated zone. The problem facing us now is that the maser beaming angle is not known. Individual rays saturate after passage through the core where they undergo exponential amplification. In the spherical geometry, only a fraction of the rays pass through the core, thus defining the radiation beaming angle. In the filamentary maser, on the other hand, *all* the rays that cross from one half to the other pass through the core and the geometry does not define a beaming angle. As a first approximation, the contribution to $J_\nu(z)$ of rays originating from the sidewall can be neglected, thus identifying the cap solid angle as the beaming cone (Goldreich and Keeley 1972). However, unlike the unsaturated maser where the intensity varies exponentially with chord length, the intensity of the subordinate stream in a saturated region varies only as a power of the length transversed (Paper II). Side rays and cap rays thus enter the core with intensities that are not too dissimilar and are subsequently amplified by approximately the same amount. It is then entirely possible that upon comparing the contributions of cap- to siderays in the integral defining J_ν, the decrease of intensity could now be offset by the increase in angular range of integration.

Consider the $z > z_{s\nu}$ saturated region; the expressions for the $z < -z_{s\nu}$ zone can be derived from symmetry. The beaming solid angle $\Omega_\nu(z)$ is defined through the relation

$$J_\nu(z) = \frac{\Omega_\nu(z)}{4\pi} I_\nu(z, \mu = 1) \tag{3.2}$$

(see eq. [II.2.4]). Although the cap solid angle need not necessarily be the beaming angle of the maser radiation, this angle still defines the essence of the filamentary geometry, and the ratio of $\Omega_\nu(z)$ to this solid angle is some dimensionless unknown function which we denote $\omega(z)$. This function specifies completely the filamentary maser solution, and in Appendix A we derive the integral equation that defines $\omega(z)$ and devise an iteration scheme to solve it. The iteration procedure starts with a trial constant function ω_1, so that

$$\Omega_\nu(z) = \omega_1 \frac{A}{(\ell + z)^2} \, . \tag{3.3}$$

Together with the beaming relation (eq. [3.2]), this specifies completely the relation between J_ν and I_ν, thus allowing a complete solution in terms of the unknown constant ω_1. This coefficient is then determined from the self-consistency condition that $J_\nu = \int I_\nu \, d\Omega/4\pi$.

The rest of this paper is devoted to this first-order solution. The approach and the methods developed here are then used in Appendix A to derive the integral equation for the full function $\omega(z)$ from the same self-consistency considerations. The accuracy of the first iteration is assessed from the second-order iteration, performed in Appendix A. The second-order corrections to quantities with direct relevance to observations are displayed in relations collected in the summary section, § VI.

The maser beaming solid angle can also be written as $\pi\vartheta_v^2$, where in the first order

$$\vartheta_v(z) = \frac{\omega_1^{1/2} R}{\ell + z} = \vartheta_{sv} \frac{\ell + z_{sv}}{\ell + z} \tag{3.4}$$

and where $\vartheta_{sv} = \omega_1^{1/2} R/(\ell + z_{sv})$ is the beaming angle at the edge of the saturated zone. The beaming angle is simply equal to the cap opening angle with the filament radius rescaled according to $R \to \omega_1^{1/2} R$, thus the value of ω_1 must obey $1 \le \omega_1 \le 4$. The lower limit arises because the contribution of side rays amounts to an effective increase in the cap radius while the upper limit is set from the requirement that at $z = \ell$ the beaming angle cannot exceed the opening angle of the rays originating at $-z_{sv}$.

The equation of radiative transfer is

$$\frac{dI_v}{dz} = \kappa_v I_v + \kappa_{0v} S_0 \tag{3.5}$$

(see eq. [I.2.19] and subsequent discussion). When applied to the dominant ray $I_v(z, \mu = 1)$ in the saturated domain, the source function can be neglected. With the aid of the beaming relation (eq. [3.2]), this then becomes an equation for the angle-averaged intensity $J_v(z)$ (see eq. [II.2.9]). An important consequence is that the resulting equation does not contain the unknown coefficient ω_1. Inserting the expression for the saturated absorption coefficient

$$\kappa_v = \kappa_{0v} J_s / J_v \tag{3.6}$$

(e.g., eq. [II.3.11]) leads to the following solution for $J_v(z)$:

$$(\ell + z)^2 J_v(z) = (\ell + z_{sv})^2 J_s + \tfrac{1}{3} J_s \kappa_{0v} [(\ell + z)^3 - (\ell + z_{sv})^3] . \tag{3.7}$$

Note again the lack of explicit dependence on the coefficient ω_1; it can only affect J_v through the location of the saturation boundary z_{sv}. When the filament is sufficiently long that $\ell \gg z_{sv}$ we find that

$$J_v(\ell) = \tfrac{7}{12} J_s \kappa_{0v} \ell , \tag{3.8}$$

a result already obtained in Paper II with the aid of some plausibility arguments (see eq. [II.2.14]). The expression for $J_v(z)$ at any z can be approximated by

$$J_v(z) \simeq \tfrac{4}{7} J_v(\ell) [1 + z/\ell - 1/(1 + z/\ell)^2] . \tag{3.9}$$

This relation is adequate for all $z \gg z_{sv}$, and the consequences of the error introduced in neglecting J_s near the saturation boundary are usually negligible.

A number of quantities follow immediately from the expression for $J_v(z)$. Because the radiation is beamed, the flux obeys the standard relation $F_v(z) = 4\pi J_v(z)$ (e.g., eq. [II.2.5]) and so

$$F_v(z) \simeq \tfrac{4}{7} F_v(\ell) [1 + z/\ell - 1/(1 + z/\ell)^2] , \tag{3.10}$$

where

$$F_v(\ell) = 4\pi J_v(\ell) = (\tfrac{7}{12}) 4\pi J_s \kappa_{0v} \ell . \tag{3.11}$$

The cap luminosity $L_{v,\mathrm{cap}}$ is simply

$$L_{v,\mathrm{cap}} = A F_v(\ell) = (\tfrac{7}{12}) h\nu \Phi_{mv} V_{1/2} , \tag{3.12}$$

where $\Phi_{mv} = 4\pi\kappa_{0v} J_s/h\nu$ is the volume production rate of maser photons (see eq. [I.2.11] and $V_{1/2}$ $(= A\ell)$ is the half-volume of the filament. Only a fraction $\frac{7}{12}$ (or 58%) of the radiation generated inside the filament is emitted through its caps. *A full* 42% *is always emitted through the side wall of the saturated filament, whatever its length or radius* (in Appendix A we show that this fraction increases to 51% in the second iteration.) For this reason, the filamentary maser solution will never correspond exactly to that of a linear maser, even when the $R \to 0$ limit is taken.

Since J_v is known, the absorption coefficient is known too (eq. [3.6]) and another quantity that can be fully determined at this point already is the intensity of subordinate rays; in the right saturated zone those are the rays that travel to the left ($\mu < 0$ for $z > z_{sv}$). This can be determined from the radiative transfer equation (eq. [3.5]) after inserting in it the complete expression for the absorption coefficient (obtained from eqs. [3.6] and [3.7]) and retaining the source function. The equation can be solved because its boundary condition is known—the intensity of a subordinate ray is zero at its entry to the maser. Of particular importance is $I_{v<}(z_{sv}, z_i)$, the intensity at the saturation edge of subordinate rays that originated on the filament surface at $z_i \gg z_{sv}$. The filamentary condition (eq. [2.12]) ensures that this intensity is independent of location on either the saturation plane ($z = z_{sv}$) or the plane of origin ($z = z_i$). A straightforward integration of the equation of radiative transfer together with equation (3.7) produces

$$I_{v<}(z_{sv}, z_i) = \frac{S_0 (\kappa_{0v} \ell)^2}{12} \left[\left(1 + \frac{z_i}{\ell} \right)^4 - \frac{4 z_i}{\ell} - 1 \right] . \tag{3.13}$$

The assumptions $z_{sv} \ll \ell$ and $\kappa_{0v} \ell \gg 3$ were made in deriving this result; both are justified in all cases of interest. The intensity of subordinate rays that originated from the cap can be obtained from this relation using $z_i = \ell$.

It is evident that much of the solution is fully determined even before the value of the unknown constant ω_1 is derived. The mere fact that the radiation is beamed suffices to determine many quantities; the precise value of the beaming angle is irrelevant for J_v, F_v and the subordinate intensity $I_{v<}$. But the dominant-ray intensity does depend on the exact value of the beaming angle, and ω_1, because

$$I_v(z, \mu = 1) = \frac{4 J_v(z)}{\vartheta_v^2} = \frac{4}{\omega_1 R^2} (\ell + z)^2 J_v(z) . \tag{3.14}$$

The equation of radiative transfer cannot be solved for the dominant ray because unlike the subordinate ray, its boundary condition is not known—the dominant ray intensity depends on the unknown beaming angle upon entry to the saturated zone at $z = z_{sv}$. An approximate expression for the z-dependence of the intensity can be written by inserting J_v from equation (3.9). The result is

$$I_v(z, \mu = 1) \simeq \tfrac{1}{7} I_v(\ell, \mu = 1) [(1 + z/\ell)^3 - 1] , \tag{3.15}$$

which demonstrates explicitly that the only undetermined quantity is the emergent intensity at $z = \ell$. Thus, the only relevant quantity with direct dependence on the unknown constant ω_1 is the intensity of the dominant ray, i.e., the maser brightness temperature.

The value of ω_1 can be determined from the condition $J_v = \int I_v \, d\Omega/4\pi$. This integral can be performed only after the angular distribution of I_v has been determined.

a) Radiation Angular Distribution

In determining the radiation angular distribution, consider the $\mu > 0$ intensity at a point $z \gg z_{sv}$ on the filament axis in the

right saturated zone. I_ν varies with direction μ because the intensity depends on the location $-z_i$ of the ray origin in the left half of the filament (Fig. 1; rays that did not pass through the core can be neglected, obviously.) Because the core segments of the rays have approximately the same length, irrespective (to the leading order in ϑ_0/ϑ_r when $z \gg z_{sv}$) of the inclination angle, all rays are amplified by the same amount during their passage through the core. Upon emergence from the core, the ratio of intensities is unchanged during travel in the right saturated zone, as can be seen from equation (3.5): for the dominant rays, the S_0 term is negligible and κ_ν ($\propto 1/J_\nu$; eq. [3.6]) is the same for all rays. Therefore, the angular distribution at z is determined exclusively by the z_i-dependence of $I_{\nu<}(-z_{sv}, -z_i)$, the intensity at the core's left boundary of a ray traveling to the right that originated at $-z_i$. But from the symmetry of the model,

$$I_{\nu<}(-z_{sv}, -z_i) = I_{\nu<}(z_{sv}, z_i) \tag{3.16}$$

and equation (3.13) therefore provides the intensity of the rightward-moving rays as they enter the core from the left. It is useful to introduce the dimensionless variable

$$\zeta = \frac{z_i}{l} \tag{3.17}$$

which varies from nearly 0 (for rays that entered at the left-saturated edge, assuming $z_{sv} \ll \ell$) to 1 (for rays originating from the left cap). At every point $z > 0$ on the axis the variable ζ is directly related to ϑ, the inclination angle of rays originating at $-z_i$, through

$$\zeta = \frac{2\vartheta_0}{\vartheta} - \frac{z}{\ell} . \tag{3.18}$$

The intensity of subordinate rays (eq. [3.13]) thus defines a distribution function

$$\Theta_1(\zeta) = [(\zeta + 1)^4 - 4\zeta - 1]/11 , \tag{3.19}$$

normalized to 1 at $\zeta = 1$. At point z on the axis, the angular distribution of radiation moving to the right is therefore

$$I_\nu(z, \vartheta) = I_\nu(z, \mu = 1) \times \begin{cases} 1 & 0 \le \vartheta \le R/(\ell + z) , \\ \Theta_1(\zeta) & R/(\ell + z) \le \vartheta \le R/z , \end{cases} \tag{3.20}$$

where ζ is related to ϑ according to equation (3.18) and $I_\nu(z, \mu = 1)$ is given in equation (3.14). We have derived the complete intensity distribution on the axis. And thanks to the filamentary condition (eq. [2.12]), *this is the intensity distribution anywhere in the saturated zone.* This distribution applies irrespective of the cross-section shape as long as it is expressed in terms of the variable ζ. The unknown coefficient ω_1 can be finally determined since the angle-averaged intensity J_ν can be calculated explicitly. For example, at the exit point $z = \ell$ the integration range $0 \le \vartheta \le \vartheta_0$ corresponds to cap rays, leading to

$$J_{\nu,\mathrm{cap}} = (\Omega_0/4\pi) I_\nu(\ell, \mu = 1) , \tag{3.21}$$

similar to the result for the unsaturated maser (when the filamentary condition is obeyed.) The range $\vartheta_0 \le \vartheta \le 2\vartheta_0$ ($1 \ge \zeta \ge 0$) corresponds to rays that originated from the sidewall, leading to

$$J_{\nu,\mathrm{side}} = 2\vartheta_0^2 I_\nu(\ell, \mu = 1) \int_0^1 \Theta_1(\zeta)(1 + \zeta)^{-3} \, d\zeta . \tag{3.22}$$

The integration is straightforward, and the result is

$$J_{\nu,\mathrm{side}} = \frac{5}{11} \left(\frac{\Omega_0}{4\pi}\right) I_\nu(\ell, \mu = 1) . \tag{3.23}$$

The contribution of the siderays is significant—about 45% that of the caprays, irrespective of the filament dimensions. Combining the cap and side contributions, the angle-averaged intensity is

$$J_\nu(\ell) = \frac{16}{11} \left(\frac{\Omega_0}{4\pi}\right) I_\nu(\ell, \mu = 1) . \tag{3.24}$$

This result agrees with the expression assumed for the beaming angle (eq. [3.2]). Thus the model is self-consistent and the coefficient ω_1 is finally determined:

$$\omega_1 = \frac{16}{11} . \tag{3.25}$$

The emitted radiation is beamed into a cone with an opening angle $\omega_1^{1/2}\vartheta_0$ and so the beaming factor of a filamentary maser is

$$\Omega_\nu/4\pi = \omega_1 \times (\Omega_0/4\pi) = 1/(11a^2) . \tag{3.26}$$

The maser intensity emitted along the axis is

$$I_\nu(\ell, \mu = 1) = \frac{4\pi}{\Omega_\nu} J_\nu(l) = \frac{77 J_s \kappa_{0\nu} \ell^3}{12R^2} . \tag{3.27}$$

This can be considered the main result of the discussion since it provides the observed brightness temperature of a filamentary maser in terms of the model parameters. Specifically,

$$kT_b = \left(\frac{77}{24}\right) \frac{\lambda^2 h\nu}{4\pi} \Phi_{mv} Ra^3 . \tag{3.28}$$

Because the brightness temperature is the only radiative quantity with explicit dependence on ω_1, this is the only relevant expression where the first-order solution differs from that of Goldreich and Keeley (1972). The brightness temperature calculations of H_2O masers in the EHM model employed a factor f for possible corrections to the Goldreich and Keeley solution. It is evident that $f = 1/\omega_1 = 11/16$. The second-order iteration performed in Appendix A reduces the value of f by an additional factor 0.84. This 16% variation in successive iterations can be considered an accuracy measure of the first-order solution.

The complete solution enables us to calculate the flux vector $\boldsymbol{F}_\nu$ at any position in the saturated zone. This is done in Appendix B, which shows that at the overall accuracy level of the first iteration,

$$\boldsymbol{F}_\nu(z, r) = F_\nu(z)\left(\boldsymbol{e}_z + \boldsymbol{e}_r \frac{r}{\ell + z}\right) \tag{3.29}$$

where $F_\nu(z)$ is given in equation (3.10), and $\boldsymbol{e}_z$ and $\boldsymbol{e}_r$ are unit vectors in the z- and r-directions, respectively. Consistent with the filamentary assumption, the magnitude of $\boldsymbol{F}_\nu$ is constant on planes of fixed z to order $1/a^2$. The presence of a small flux component in the cylindrical radial direction implies that off the main axis, the direction of the flux is slowly diverging away from the z-direction. However, even on the cylinder sidewall ($r = R$), the flux vector is pointed almost exactly along the main axis, the deviation from this direction never exceeding $2\vartheta_0$. The sidewall luminosity of each maser half is obtained

from

$$L_{\nu,\text{side}} = \int_0^{\ell} \boldsymbol{e}_r \cdot \boldsymbol{F}_\nu(z, R) 2\pi R \, dz \, . \tag{3.30}$$

The flux through the sidewall is smaller than through the cap, by $\sim 1/a$, but the area is larger by the same factor. With the aid of equations (3.29), (10), and (11) we find

$$L_{\nu,\text{side}} = (5/7) A F_\nu(\ell) = (5/12) h\nu \Phi_{m\nu} V_{1/2} \, . \tag{3.31}$$

Together with equation (3.12) this shows that all the luminosity generated inside the filament is properly accounted for and carried through the caps and sidewall by the calculated flux, thus providing another self-consistency check of the first-order solution. The flux vector field also enables us to calculate the flux lines, the curves whose tangent at any point is in the direction of the local flux vector. These lines are obtained from the equation $dr:dz = F_r:F_z$, and it follows immediately that they are described by the equation

$$r = r_0(1 + z/\ell) \tag{3.32}$$

for $z \geq 0$, where r_0 is the value of r on the central plane; the lines for $z \leq 0$ are obtained by mirror reflection. Thus the flux lines are simply straight lines emanating from the $z = 0$ plane in both directions. An analytic continuation of the flux lines from the filament right-half to negative values of z shows that they all converge toward the point ($z = -\ell$, $r = 0$)—the center of the opposite cap. The center of each cap is therefore the flux divergent point for the opposite half of the filament. This property was used in Paper II for a derivation of equation (3.8) based on the Gauss theorem.

b) Core Properties

The length of the core is determined from the condition that the axial ray that enters on one end as a subordinate ray emerge on the other as the dominant ray due to exponential amplification. For the ray that travels to the right, the intensity at core entry, assuming $\ell \gg z_{s\nu}$, is

$$I_\nu(-z_{s\nu}, \mu = 1) = \tfrac{11}{12} S_0 (\kappa_{0\nu}\ell)^2 \, , \tag{3.33}$$

as can be easily seen from equations (3.13) and (3.16). Upon emergence from the core its intensity is

$$I_\nu(z_{s\nu}, \mu = 1) = \frac{11 J_s \ell^2}{4R^2} \, , \tag{3.34}$$

as evident from equation (3.14). The amplification across the core, the ratio of these two intensities, is therefore

$$\exp(2\kappa_{0\nu} z_{s\nu}) = \frac{3\gamma}{(\kappa_{0\nu} R)^2} \, . \tag{3.35}$$

As mentioned in § II, our models for H_2O masers in star-forming regions (EHM) produce typical values of $\kappa_{0\nu} R \simeq 4$ while γ is usually $\sim 10^6$ (see also Paper I). Therefore, $z_{s\nu} \simeq 1.5R \ll \ell$, as assumed.

In contrast with the result for a linear maser ($\kappa_{0\nu} z_{s\nu} = \ln[2\gamma^{1/2}/\kappa_{0\nu}\ell]$; eq. [I.3.15]), the saturation boundary of the filamentary maser is independent of ℓ, although it varies with R. The reason for this is that the ℓ-dependences of $I_\nu(-z_{s\nu}, \mu = 1)$ and of $\vartheta_{s\nu}^2$ are the inverse of each other (when $\ell \gg z_{s\nu}$). But R cannot be varied at will because the filamentary condition must always be obeyed. It is therefore more appropriate to express the saturation boundary in terms of the filament length ℓ and aspect ratio a as

$$\kappa_{0\nu} z_{s\nu} = \ln \frac{a(3\gamma)^{1/2}}{\kappa_{0\nu}\ell} \, . \tag{3.36}$$

Varying the filament length while a is kept fixed provides similar behavior to the linear maser.

The filament beaming angle is nearly constant across the core when $z_{s\nu} \ll \ell$. The relation between $J_\nu(z = 0)$ and J_s is thus similar to that for a linear maser, namely,

$$J_\nu(0) = 2J_s \exp(-\kappa_{0\nu} z_{s\nu}) \, . \tag{3.37}$$

Complete core saturation occurs when $J_\nu(0) = J_s$, or $\exp(\kappa_{0\nu} z_{s\nu}) = 2$. Combined with equation (3.35), the condition for complete saturation is that the radius exceed the value obtained from

$$\kappa_{0\nu} R_{c\nu} = \tfrac{1}{2}(3\gamma)^{1/2} \, . \tag{3.38}$$

Again, it is more appropriate to consider this as a relation for the length at a fixed aspect ratio

$$\kappa_{0\nu} \ell_{c\nu} = \tfrac{1}{2} a (3\gamma)^{1/2} \, . \tag{3.39}$$

During complete saturation, the core boundary z_c can be obtained from equation (II.3.23). The beaming angles at z_c are $\vartheta_{+c} = \vartheta_{-c} = 2\vartheta_\nu(\ell)$ where $\vartheta_\nu(\ell) = \omega_1^{1/2}\vartheta_0$. Therefore,

$$z_c = \frac{4\ell\vartheta_0}{(3\gamma)^{1/2}} = \frac{2R}{(3\gamma)^{1/2}} \, . \tag{3.40}$$

It is evident from these results that our models for H_2O masers in star-forming regions (EHM) are not even close to complete saturation since $\kappa_{0\nu} R$ is only ~ 4 while $\gamma \sim 10^6$. In addition, as noted already in Paper I, the properties of the core have no effect on the solution in the end regions $|z| > z_c$. The maser's observed features, in particular the brightness temperature, are the same whether the core is saturated or not. Core saturation is therefore mostly a matter of pure theoretical interest.

IV. EXTERNAL RADIATION AND INTERACTING FILAMENTS

The only source of input radiation considered so far was spontaneous decays inside the maser itself. In this section we add the effects of an external source with intensity I_e, located along the axis of a filamentary maser (Fig. 2*a*). The source is assumed to be sufficiently distant that the angle $\vartheta_e (< \vartheta_0)$ it subtends at the maser can be considered constant throughout the filament. When the maser is unsaturated, the effect of the background radiation is always described by equation (2.4), irrespective of the geometry. As pointed out in Paper I, the intensity modification is comprised in this case of $S_0 \to S_0 + I_e$ and the effect of the background source on the solution is thus measured by

$$\gamma_e = I_e/S_0 = T_e/T_{x0} \, , \tag{4.1}$$

where T_e is the brightness temperature of the external source and T_{x0} is the unsaturated maser excitation temperature. A maser in front of a background source displays emission which is enhanced over the value it would have had if that source was not there. An enhancement factor χ can be defined as

$$\chi \equiv \frac{I_\nu}{I_{\nu nb}} \, , \tag{4.2}$$

where the subscript *nb* denotes the intensity in the absence of external radiation. Evidently, for an unsaturated maser

$$\chi = 1 + \gamma_e \,. \tag{4.3}$$

The enhancement is thus determined exclusively by the parameter γ_e in this case.

While an analytic solution is not available in any three-dimensional geometry, the full solution in the linear case was developed in detail in Paper I, and we can rely upon it for guidance in the filamentary geometry. Some caution must be exercised, however. The linear maser does not have a true intensity; the functions $I_{\nu\pm}$ are actually angle-averaged intensities (Paper I; see also Appendix C). Thus the linear maser solution provides a correct indication of the behavior of J_ν but not of I_ν. As in the linear case, external radiation can only increase the maser J_ν by up to factor of 2 when the core moves all the way to the filament edge and the saturated volume is doubled; luminosity enhancements of more than a factor of 2 are thus precluded by fundamental maser properties. But the intensity I_ν can be enhanced indefinitely along selected rays, as long as their overall contribution to J_ν is negligible. The unsaturated core and the right-saturated zone amplify input radiation by some given amount. Rays that enter the core with a higher intensity, such as those originating from the external source, will therefore emerge stronger. Thus the external source can appear arbitrarily bright even through a saturated maser—provided its angular extent is sufficiently small.

Consider now the filamentary solution in the absence of external radiation (previous section). The intensities at core entrance of the external and internally generated radiation, $I_{\rm ex}$ and $I_{\rm in}$, respectively, calculated in this unperturbed solution are

$$I_{\rm ex} = 7/3\; I_e \kappa_{0\nu} \ell \,, \quad I_{\rm in} = 11/12\; S_0 (\kappa_{0\nu}\ell)^2 \,, \tag{4.4}$$

as can be easily shown from the results of § III. The contributions to J_ν at the core entry of these two components will be denoted $J_{\rm ex}$ and $J_{\rm in}$, respectively. These contributions are obtained by multiplying each of the intensities by the appropriate solid angle factor—$1/4\vartheta_e^2$ for the external radiation and $16/11\vartheta_0^2$ for the internally generated radiation. The ratio of these two components of J_ν

$$\mathscr{R}_e = \frac{J_{\rm ex}}{J_{\rm in}} = \frac{7}{16}\,\frac{\gamma_e}{\kappa_{0\nu}\ell}\left(\frac{\vartheta_e}{\vartheta_0}\right)^2 \tag{4.5}$$

controls the structure of the solution (Paper I); in particular, the core shifts to the left by the amount $\ell\mathscr{R}_e/(1+\mathscr{R}_e)$ (see eq. [I.4.17]). Therefore, $\mathscr{R}_e/(1+\mathscr{R}_e)$ is the fractional increase in volume of the right saturated zone due to the external radiation, and hence the fractional increase in J_ν at exit on the right. The fractional increase in intensity emerging toward the observer is obtained after scaling by the appropriate ratio of the two beaming factors, leading to

$$\chi = 1 + \frac{64}{11}\left(\frac{\vartheta_0}{\vartheta_e}\right)^2 \frac{\mathscr{R}_e}{1+\mathscr{R}_e} \tag{4.6}$$

(see eq. [I.4.18]). This is the general result for the enhancement factor. It holds as long as the intensity of the external radiation is not so high as to cause saturation by itself without any further amplification in the left saturated zone; that is, the validity range of this expression is $1/4\vartheta_e^2 I_e < J_s$, which is always obeyed in practice.

Although the expression for χ was derived by inference from the linear maser solution, it provides the correct result in two limits where a solution is available. When $\mathscr{R}_e \ll 1$,

$$\chi = 1 + \frac{28}{11}\,\frac{\gamma_e}{\kappa_{0\nu}\ell} \,, \tag{4.7}$$

a result which is easy to understand: In this limit, $J_{\rm ex} \ll J_{\rm in}$ and the maser structure is unaffected by the external radiation. The terms $I_{\rm ex}$ and $I_{\rm in}$ of equation (4.4) are then the actual intensities at core entrance of the external and internally generated radiation, respectively. These intensities maintain their relative strengths during further amplification while traveling through the core and the right saturated zone. Their ratio therefore provides the ratio of emerging intensities with and without background radiation—the maser enhancement factor; hence equation (4.7). This result can also be derived by calculating the emergent intensity from $I_e \exp \tau_\nu(-\ell, \ell)$ using the expression derived in Paper II for the overall gain of an unperturbed saturated maser (eq. [II.3.17]). As expected, the enhancement can increase with γ_e without bound, but because of the condition $\mathscr{R}_e \ll 1$ such unrestricted amplification is confined to small angles. Note that this condition also ensures that the luminosity of the amplified external radiation is smaller than the internally generated maser luminosity, so the overall luminosity cannot increase by more than a factor of 2. Because this added luminosity is confined to a much smaller angle, the intensity can be accordingly higher.

The condition $\mathscr{R}_e \ll 1$ is obeyed whenever the external source is either weak or distant. The other limit is $\mathscr{R}_e \gg 1$, and the corresponding enhancement factor is

$$\chi = 1 + \frac{64}{11}\left(\frac{\vartheta_0}{\vartheta_e}\right)^2 . \tag{4.8}$$

The maser structure is controlled now by the external radiation since $J_{\rm ex} \gg J_{\rm in}$. Because J_ν is dominated by the external component, the beaming angle is constant throughout the filament (on account of the assumption that the external source is distant) and the maser acts effectively as a linear maser. It is easy to solve the radiative transfer equation in this case and show that except for a correction factor of 6/7, the solution is identical to the result of equation (4.8); this is an indication of the accuracy of our general result, equation (4.6). The maser luminosity is only enhanced by $\sim 50\%$.

a) Interacting Filaments

Consider now the situation when the external source is itself a filamentary maser, with radius R_b and half-length ℓ_b, respectively, its axis aligned with the foreground maser at a distance d (Fig. 2*b*). The internal properties of the background filament (pump rates, etc.) are assumed identical. The external intensity I_e is then obtained from equation (3.27) and the angle ϑ_e is R_b/d. Therefore, $\mathscr{R}_e = (d_i/d)^2$ where

$$d_i = a\ell_b (11\gamma\ell_b/\ell)^{1/2} \tag{4.9}$$

defines a distance scale for the interacting pair (a factor of 49/48 inside the square root has been set to unity.) The masers affect each other's structure so long as their separation is smaller than the interaction distance d_i. For masers with identical lengths the distance d_i obeys

$$d_i/\ell = 10^3 a \gamma_5^{1/2} \,, \tag{4.10}$$

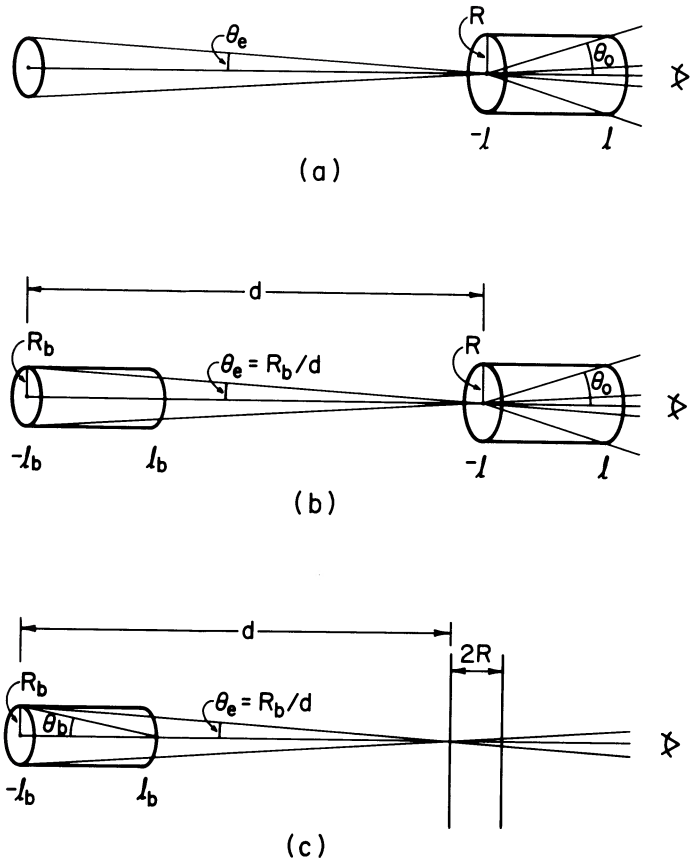

FIG. 2.—Maser amplification of background radiation: (*a*) a filament amplifying a distant source, (*b*) a filament amplifying a background filament, and (*c*) a background filament amplified by a foreground slab.

where $\gamma_5 = \gamma/10^5$. This is a rather large distance. The reason interaction can persist to such large separations is that in each filament, it is the subordinate intensity which has to compete with the dominant intensity of the other member of the pair. If T_{b1} denotes the brightness temperature (obtained from eq. [3.28]) of the foreground maser acting as a single filament, the brightness temperature T_{b2} of the interacting pair is

$$T_{b2} = T_{b1}\left[1 + \frac{16}{11}\left(\frac{R}{R_b}\right)^2\left(\frac{d}{\ell}\right)^2 \frac{d_i^2}{d^2 + d_i^2}\right]. \quad (4.11)$$

When the filament separation is much less than d_i, the brightness temperature increases with separation in proportion to $(d/\ell)^2$. Even though these results were derived under the assumption that $d \gg \ell$ (to ensure a constant ϑ_e), the limit $d \to 2\ell$ for identical filaments produces an enhancement factor of 6.8, reasonably close to the correct answer $\chi = 8$ (the two filaments are then simply joined to form a maser with double the length). When $d \gg d_i$, the brightness temperature approaches the limit

$$T_{b,\max} = T_{b1}\, 16\gamma a_b^2 \ell_b/\ell = (154/3k)\lambda^2 J_s \kappa_{0\nu} \ell_b \gamma a^2 a_b^2 \quad (4.12)$$

where a_b is the aspect ratio of the background maser. This is the maximal brightness temperature that can be produced by two aligned filaments, obtained when their separation is sufficiently large that they do not affect each other's structure. From equation (4.10), the filaments' separtion must be substantial before this limit is reached.

These results are easy to understand. The brightness temperature of a filamentary maser is proportional to $\ell \times (\ell/R)^2$, with the first factor reflecting the size of the emitting volume (hence the luminosity) and the second one the beaming angle of the radiation. As long as $d \ll d_i$ the two members of the pair can simply be considered the two halves of a single filament, separated by a distance d. This does not affect the first factor, since the radiation producing volume does not change, thus the overall luminosity hardly changes by such separation (small changes reflect the motion of the core location inside each filament). But the beaming angle is now tighter, proportional to R/d instead of R/ℓ, and so the brightness temperature increases in proportion to $\ell(d/R)^2$. Equivalently, the two masers can be considered a single lengthy filament with overall length d whose midsection has been removed; this removal affects only the radiation generation volume, not the beaming angle, producing the same result. It should be noted that at a large distance $D(\gg d)$, the observed angular size of either maser is R/D—much smaller than and unrelated to the beaming angle. Thus the observed size of the interacting pair is the same as that of the background filament acting as a single maser. Once the pair separation exceeds the interaction distance d_i, the structures of the masers are those of two isolated filaments and the pair can no longer be considered the two halves of a single maser. The brightness temperature reaches the maximum of equation (4.12), since further separation has no effect on either the intensity entering each filament or their overall gains. The pair excess luminosity is decreasing as $(R/d)^2$ because of the smaller angle occupied by the radiation that arises from their interaction.

Interacting filaments have been studied recently by Deguchi and Watson (1989). They proposed that the single-filament brightness temperature is enhanced by a factor near $(d/\ell)^2$ as long as the radiation of the other maser is the dominant source of stimulated emission. This requirement is equivalent to $d \ll d_i$, and their proposal is in agreement with equation (4.11) in this limit.

b) H_2O *Maser Bursts*

We propose that maser amplification of input maser radiation is the explanation for the giant burst sometimes observed in H_2O maser emission from star-forming regions (Matveenko 1986). Two events have been reported so far, one in W49 (Burke et al. 1973) the other in Orion (Abraham et al. 1981). In both cases the sources flared up, leading to a very high brightness temperatures ($T_b > 10^{15}$ K) and unusually small dimensions and linewidths (Matveenko 1986; Garay, Moran, and Haschick 1989). In the case of Orion at least, this was also coupled with high linear polarization (up to 70%; Garay et al.) These are clearly unique events that require their own explanation, different from that of other H_2O maser features.

Our model for H_2O masers behind shocks in star-forming regions produces single-filament brightness temperatures of

$$T_{b1} = 0.9 \times 10^{12}(a/10)^3 \text{ K} \quad (4.13)$$

(eq. [2.3] of EHM with proper account for the factor of f, including the second-order correction). Observations show that individual features in H_2O maser sources typically have brightness temperatures in the range $\sim 10^{12}$–10^{13} K (Genzel 1986), and can therefore be explained with aspect ratios in the range $\sim$10–20. Occasionally, brightness temperatures of $\sim 10^{14}$ K are detected, and those would require that some filaments have aspect ratios as high as $\sim$50. A phenomenologi-

cal analysis of the observations shows that the data are indeed suggestive of a description in terms of filaments with a distribution of aspect ratios in this range (Genzel 1986). We therefore propose that with the possible exception of the burst events, all the observed H_2O maser emission from Galactic sources can be explained as the result of internally generated radiation in single filaments. Brightness temperatures in excess of 10^{15} K, observed in the burst events, require the occurrence of either extreme aspect ratios, in excess of 100, or the chance alignment of two filaments that can then amplify each other's radiation, as described above. Both alternatives involve low probability situations, but then they only need apply to two unique events. So far, extreme brightness temperatures were recorded only in burst events with distinctive properties, suggesting that there is a dichotomy in the data between $T_b \lesssim 10^{14}$ K and $T_b > 10^{15}$ K. This indicates to us that the explanation based on chance alignment of two masers should get preference.

The chance alignment of filament pairs provides an adequate explanation for the giant bursts, with the extreme brightness temperatures requiring an enhancement factor of $\chi \sim 100$. As can be seen from equation (4.12), with $\gamma \sim 10^5$ and $a \sim 10$ the enhancement can reach as much as $\chi \sim 10^8$—considerably more than what is needed (or observed, so far). However, this limit is only approached at filament separations that exceed their lengths by 10^4 (eq. [4.10]), much more than the overall dimensions of maser regions. Astronomical maser sources are always confined to $d \ll d_i$ where the enhancement is

$$\chi = \frac{16}{11}\left(\frac{R}{R_b}\right)^2\left(\frac{d}{\ell}\right)^2 \tag{4.14}$$

(eq. [4.11]). An enhancement of $\chi \sim 100$ is produced when the filaments' separation is 10 times their length. An alignment of this type is not unreasonable for filament opening angles of $\vartheta_0 \sim 1/10$. In our model the filament lengths range from $\sim 10^{14}$ to $\gtrsim 10^{15}$ cm so the filament separation would have to be $\gtrsim 10^{15}$–10^{16} cm, in accord with observed dimensions of groups of maser spots. The small dimensions and line widths of the burst sources can be attributed to the additional constraints imposed by the alignment. Maser features are usually small and have narrow lines because of the restrictions imposed by velocity coherence. These become even more stringent when two filaments have to cooperate. Note that $R_b < R$ only adds to the enhancement (eq. [4.14]). The time variability of intensity and line width observed in the Orion burst (Garay et al.) can be attributed to fluctuations in the degree of alignment. The high polarization observed in this burst requires the presence of aligned magnetic field in the source. If the cause of this burst was indeed filament alignment, it is tempting to speculate that it resulted from effects related to magnetic interaction.

A different type of amplification occurs when maser radiation is passing through an unsaturated maser. Such a situation is likely in our model because the filaments reside in sheetlike shocked regions whose thickness is equal to the filaments' diameters (Fig. 2*c*). Unsaturated amplification can occur when the line of sight to a given filament intersects a shocked slab face-on. If the slab's perpendicular gain is τ ($=2\kappa_0 R$ where R is a typical filamentary radius) then the filament's intensity is amplified by $\chi = e^{\tau}$ before reaching the observer and an enhancement by $\chi = 100$ requires only $\tau = 4.6$ ($\kappa_0 R = 2.3$). As mentioned before, our model produces $\kappa_0 R \simeq 4$ for prototype filaments so such amplification does not pose any problem and is obtained at slab thickness of only $\sim 1.4 \times 10^{12}$ cm. However, since the overall gain of an unsaturated maser is smaller than for a saturated maser, χ cannot exceed the saturated results. Indeed, unsaturated amplification is constrained by the requirement that inside the slab itself, the contribution of the amplified radiation to the angle-averaged intensity not exceed the saturation intensity J_s, otherwise the slab's illuminated region would saturate. Using the results of § III it is easy to show that this requirement limits the unsaturated amplification to

$$\chi \lesssim \frac{192}{77}\left(\frac{\vartheta_b}{\vartheta_e}\right)^2 \frac{1}{\kappa_{0\nu}\ell_b}, \tag{4.15}$$

where ϑ_b is the opening angle of the background filament (Fig. 2*c*). As expected, this is indeed smaller than the corresponding saturated amplification (see eq. [4.8] for identical filaments). This constraint can be expressed as a lower bound on the filament-slab separation

$$(d/\ell_b)^2 \gtrsim 77/48\ \kappa_{0\nu} R_b \chi a_b\ . \tag{4.16}$$

When this limit is exceeded, the slab saturates and the previous treatment applies. Inserting representative values we find

$$d/\ell_b \gtrsim 80[(\kappa_{0\nu} R_b/4)(\chi/100)(a_b/10)]^{1/2}\ . \tag{4.17}$$

Therefore, the separation in a filament-slab configuration must be about an order of magnitude larger than filament-filament to achieve comparable enhancement. Such separations ($\sim 10^{16}$–10^{17} cm) are still compatible with observed dimensions of groups of maser features.

This analysis shows that both saturated and unsaturated amplifications are capable of explaining the brightness temperatures of H_2O giant burst events with plausible parameters. Although unsaturated amplification requires an alignment at larger separation, the foreground element of the aligned pair presents a much larger target area, being a sheetlike object rather than a filament. An estimate of the comparative likelihood of these and other types of alignment requires a detailed geometrical model for the entire source, and will be done in a forthcoming paper (Elitzur, Hollenbach, and McKee 1990). Fast time variations would tend to favor unsaturated amplification because of the exponential response and shorter crossing times across a slab than along a filament. During unsaturated amplification, the radiation reaching the observer is that of an unsaturated slab amplifying a background source. Time variability is then expected to be similar to that of a radiatively pumped unsaturated maser, giving rise to fast fluctuations. In particular, the radiative crossing time determines the onset of saturation in the slab.

During the initial phase of the Orion burst, the intensity appears to have doubled in about a day (Abraham et al. 1981). With unsaturated amplification this can be attributed to an increase of $\ln 2 = 0.7$ in the gain τ. Because the dependence of gain on slab thickness (and optical depths of IR transitions) is nonlinear, the dimensions associated with such a change depend on the value of the gain. A slab whose overall perpendicular gain is $\tau = 0.7$ is only 4×10^{10} cm thick while a change in gain from $\tau = 4$ to $\tau = 4.7$ occurs during increase in slab thickness from 8×10^{11} cm to 1.5×10^{12} cm, for a thickness change of 7×10^{11} cm. At a typical shock velocity of ~ 100 km s^{-1}, the crossing time for the latter dimension is just one day and the radiative crossing time is only ~ 5 minutes; the former thickness produces time scales that are even smaller, by a full

order of magnitude. Observations may be expected to display variations on all time scales. Indeed, time scales as short as ~ 5 minutes may have been detected for intensity fluctuations in the Orion burst (Matveenko 1986). A plausible scenario for this event is that a slab intersected the line of sight to a background filament because of either the formation of a new shock front or the oblique propagation of an existing one. This provided initially unsaturated amplification (explaining the fast rise time and rapid fluctuations) that later switched to saturated amplification as a result of the interaction with the background filament.

Amplification by filament pairs as an explanation for H_2O masers in star-forming regions has been recently invoked by Deguchi and Watson (1989). Unlike the proposal made here, their model seems to imply amplification for most (if not all) of the observed features in strong sources and to require axial alignment of filament pairs. In contrast, our model requires such amplification only for the giant bursts, whose properties appear to be distinctly different from those of other features, and indicates that in the case of Orion at least, the interaction involved a foreground sheetlike maser intersecting face on the line of sight to a background filament.

V. OBSERVATIONAL IMPLICATIONS

One of the most important questions confronting any attempt at modeling of astronomical masers is the appropriate geometry to use for the underlying structure. The filamentary and spherical geometries studied here and in Paper II represent the prototypes of elongated and isotropic sources, respectively. A formal comparison of the two solutions is provided in Appendix C. It is important to find out which observations, if any, can distinguish between these different configurations, and this is done in this section.

It is instructive to digress first on the quantities that can be determined unambiguously from observations. The only radiative quantity directly measured is the observed flux $F_{\nu,\mathrm{obs}}$. It is related to the (distance independent) intensity I_ν and the solid angle subtended by the source Ω_{obs} via

$$F_{\nu,\mathrm{obs}} = I_\nu \Omega_{\mathrm{obs}} . \tag{5.1}$$

Therefore the intensity (i.e., the brightness temperature) can be directly determined from the ratio of two observable quantities. But the flux F_ν at the source *cannot* be determined from observations because the radiation is beamed and the beaming angle Ω_ν is not an observed quantity. For any source, the solid angle covered by observing instruments is minute; it is many orders of magnitude smaller than the beaming angle of maser radiation. Thus the relation

$$F_\nu = I_\nu \Omega_\nu \tag{5.2}$$

(eq. [II.2.5]) which holds at the source involves the two unobserved quantities F_ν and Ω_ν. As a result, the luminosity too is unobservable since it is the surface integral of F_ν.

If the distance D to the source is known, the observed solid angle Ω_{obs} provides the observed area

$$A_{\mathrm{obs}} = D^2 \Omega_{\mathrm{obs}} . \tag{5.3}$$

Models that produce the same brightness temperature and observed area are therefore indistinguishable by maser observations because these are the only quantities that can be determined unambiguously. The observed area of a spherical maser is just a small cap on its surface with area $R^2\Omega_\nu(R)$ (Paper II). The sphere would therefore appear identical to a cylindrical maser with radius $R\vartheta_\nu(R)$ and the same brightness temperature. The resemblance between the spherical and cylindrical masers is a close one. Consider a spherical maser with radius R and its cylindrical subvolume with radius $R\vartheta_\nu$ and length $2R$ aligned along the line of sight. This tube is virtually identical to an independent cylindrical maser of the same dimensions and with the same pump and loss rates. The observed area of both configurations is the same. The beaming angle of the independent cylinder would be $\omega_1^{1/2} R\vartheta_\nu/(2R) = 0.6\vartheta_\nu$ instead of ϑ_ν for the sphere's subregion, and its angle-averaged intensity would be $(7/12)J_s\kappa_{0\nu}R$ instead of $(1/3)J_s\kappa_{0\nu}R$. Consequently, the brightness temperatures of the two configurations differ by only 4.8. Thus, apart from numerical factors of order unity the two configurations are indistinguishable. *From any given direction, the appearance of a spherical maser is indistinguishable from that of the equivalent cylindrical maser.* The suggestion that a certain maser source is spherical therefore involves the assumption, which cannot be directly verified, that in addition to the observed cylindrical region there is a whole unobserved spherical volume with identical properties.

In both spherical and filamentary masers, observations can determine a linear scale in the transverse direction but not along the line of sight. Thus in a spherical maser the radius of the observed region $R\vartheta_\nu$ can be determined, but not the actual radius R. Likewise, the radius of a filamentary maser can be determined from observations, but not the half-length ℓ. In both cases this amounts to the fact that the beaming angle cannot be determined. The corollary is that maser gain is not a measured quantity.

In spite of the similarities, the radiation angular distribution is very different for the two configurations. In the spherical maser the distribution is determined by the length of the chord in the unsaturated core where the amplification is exponential, resulting in a Gaussian angular distribution. In the filament, on the other hand, the determining factor is the subordinate segment of the ray path, and the resulting angular distribution is a more moderate power law. This is of little consequence for observations, though.

When the distance to the source is known, it is customary to express the observed flux in terms of the isotropic luminosity $L_{\nu,\mathrm{iso}} = 4\pi D^2 F_{\nu,\mathrm{obs}}$. From the previous equations it follows that

$$L_{\nu,\mathrm{iso}} = F_\nu A_{\mathrm{obs}} \times 4\pi/\Omega_\nu . \tag{5.4}$$

The isotropic luminosity is an observed quantity (since F_ν/Ω_ν is observable) but it need not equal the actual overall luminosity, which is unobserved (the ratio F_ν/Ω_ν is observable but neither quantity in itself). The observed area of a spherical maser is $R^2\Omega_\nu$ so $L_{\nu,\mathrm{iso}} = 4\pi R^2 F_\nu$, the sphere's actual luminosity. In spite of the beaming, the isotropic luminosity of a sphere is equal to its real luminosity, an obvious result in light of the symmetry. The luminosity of a spherical maser can thus be determined from $F_{\nu,\mathrm{obs}}$ and D. It is an observationally determined quantity, only because of the assumption about the existence of an unobserved emitting volume. In the case of a filamentary maser the observed area is the cap, the beaming angle is $\pi\omega_1\vartheta_0^2$ and

$$L_{\nu,\mathrm{iso}} = (77/24)a^2 L_\nu . \tag{5.5}$$

The isotropic luminosity overestimates the source actual luminosity $L_\nu (= 2\ell A h\nu \Phi_{m\nu})$ by a rather large factor. The source

luminosity cannot be determined from $F_{\nu,\mathrm{obs}}$ and D alone without an assumption about the filament aspect ratio, equivalent to the isotropy assumption made for a spherical maser. The luminosity of the observed volume is similar for both geometries.

An important difference between the two geometries involves the frequency dependence of the beaming angle Ω_ν. The filamentary geometry is characterized by the cap solid angle, thus the beaming angle is frequency independent. A sphere, on the other hand, has only one geometrical scale, its radius, so there is no intrinsic angle defined by the geometry. The construction of an angle requires use of the length scale $1/\kappa_{0\nu}$, which is frequency dependent, and the beaming angle therefore varies with frequency, as long as the core does not saturate. The *observed size of a filamentary maser is fixed, while for a spherical maser it varies with frequency shift from line center* (Paper II). This provides an observational test to distinguish between the two geometries.

Since the appearance of a sphere is the same in all directions, the distribution of brightness temperatures of an assembly of spherical masers with identical internal properties will simply reflect the radii distribution of the population. In contrast, a filament appears different to different observers at distance D ($\gg \ell$), depending on the angle ϑ between the line of sight and the filament axis (Fig. 3). As long as $\vartheta \leq 2\vartheta_0$, the observer intersects rays that traveled the full length of the maser and the observed intensity is ϑ-independent, thanks to the filamentary condition (eq. [2.12]). When $\vartheta > 2\vartheta_0$ ($\vartheta a > 1$), the rays get shorter, and when $\vartheta > 4\vartheta_0$, only rays that exit through the sidewall are observed (since they have to originate at the left half). The solid angle of a sidewall segment dz is $d\Omega = 2Rdz \sin \vartheta/D^2$ and the sidewall contribution to the observed flux can therefore be obtained from

$$F_{\nu,\mathrm{obs}} = \frac{2R \sin \vartheta}{D^2} \int_{z_1}^{z_2} I_\nu(z, \vartheta) dz \,, \tag{5.6}$$

where z_1 and z_2 are appropriate limits. For example, when $\vartheta > 4\vartheta_0$, $z_1 = 0$ and $z_2 = 2R/\tan \vartheta$ (Fig. 3*b*). The intensity $I_\nu(z, \vartheta)$ is obtained from equations (3.15) and (3.20), and the value of z_i, required for the angular distribution $\Theta_1(\zeta)$, is obtained from $z + z_i = 2R/\tan \vartheta$. The integration is straightforward, and the leading term in the result is

$$a\vartheta \geq 2: \quad F_{\nu,\mathrm{obs}} = F_1 \frac{4R^2 \cos \vartheta}{D^2} (a \tan \vartheta)^{-3} \,, \tag{5.7}$$

where F_1 is some constant whose value may depend on the precise shape of the filament cross section. It should be noted that $4R^2 \cos \vartheta$ is simply the projection in the observer's direction of the sidewall area that allows emission in the direction ϑ (Fig. 3*b*); the observed solid angle is

$$\Omega_{\mathrm{obs}} = \frac{2R \sin \vartheta}{D^2} \int_{z_1}^{z_2} dz = 4R^2 \cos \vartheta / D^2 \,. \tag{5.8}$$

Therefore, the filament appears *smaller* at larger angles. This result, a somewhat surprising consequence of beaming, is in fact quite obvious: For an observer at angle $\vartheta = 2\vartheta_0$, the projected areas of the cap and the sidewall are equal (Fig. 3*a*). As the angle increases, the cap disappears and only a fraction of the sidewall contributes, since observed rays must have crossed through the unsaturated core (Fig. 3*b*). The observed brightness temperature ($\propto F_{\nu,\mathrm{obs}}/\Omega_{\mathrm{obs}}$) therefore obeys

$$T_b(\vartheta > 4\vartheta_0) = T_b(\vartheta = 4\vartheta_0)[2/(a \tan \vartheta)]^3 \,. \tag{5.9}$$

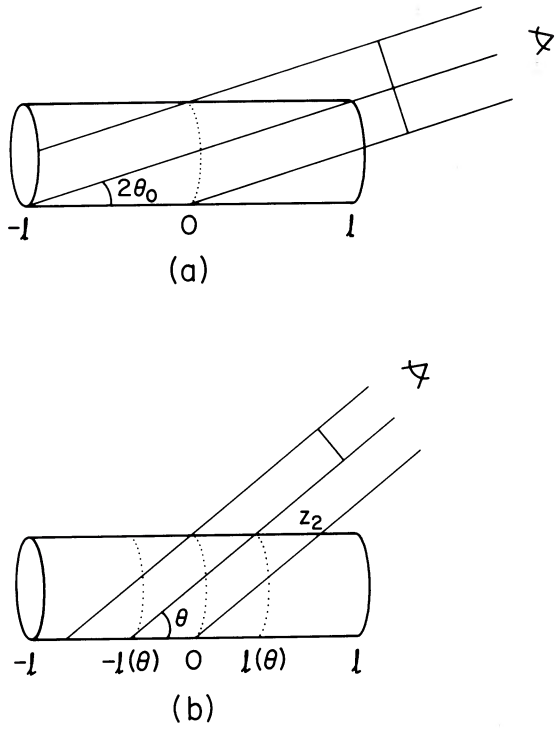

FIG. 3.—Emission toward a distant observer at an angle (*a*) $2\vartheta_0$ to the axis and (*b*) $\vartheta > 4\vartheta_0$.

The integrations in the range $2\vartheta_0 \leq \vartheta \leq 4\vartheta_0$ ($1/a \leq \vartheta \leq 2/a$) can be performed in a similar manner. The observed solid angle obeys the same relation while the result for $F_{\nu,\mathrm{obs}}$ is slightly more involved because more terms must be retained. However, the difference is not significant and this is only a small transition region anyhow. We can therefore employ the result of equation (5.9) as an approximation in this region too, and the dependence of brightness temperature on angle and aspect ratio is thus

$$T_b(a, \vartheta) \simeq T_0 a^3 \times \begin{cases} 1 & \vartheta \leq 1/a \\ 1/(a\vartheta)^3 & \vartheta \geq 1/a \,, \end{cases} \tag{5.10}$$

where T_0 is a function of the filament's internal properties and its radius; our model for H_2O masers in star-forming regions produces $T_0 \simeq 10^9$ K for typical parameters (see eq. [4.13]). In deriving this result the small angle approximation was employed; if large angles become important, ϑ should be replaced with $\tan \vartheta$. Therefore, *a filament with a large aspect ratio observed at large angles* ($\vartheta > 1/a$) *will appear as bright as filaments with smaller aspect ratios* $\sim 1/\vartheta$ *observed along the axis.* This result is easy to understand: the emission at the large angles is dominated by rays that travel comparable distances in both saturated zones, corresponding to an effective filament whose length is $l(\vartheta) = \ell/(a \tan \vartheta)$ (Fig. 3*b*).

We can now derive the histogram of brightness temperatures of a filament population, assuming they all have the same internal properties and radius (so T_0 is the same). Since the radii are the same, the variation of filament lengths generates a distribution of aspect ratios. Denote by $\mathcal{N}(a)da$ the number of filaments with aspect ratios in the range $[a, a + da]$. At an arbitrary observer location, all orientations are equally likely and the distribution in a and ϑ is $d\mathcal{N}(a, \vartheta) = \mathcal{N}(a) \sin \vartheta da d\vartheta$. We seek the distribution $d\mathcal{N}(T_b)$, the number of filaments

observed in the brightness interval $[T_b, T_b + dT_b]$. For the brightness temperature T_b, introduce the characteristic aspect ratio

$$a(T_b) = (T_b/T_0)^{1/3} . \tag{5.11}$$

Filaments with aspect ratio $a = a(T_b)$ will contribute to the brightness interval at all angles $\vartheta \leq 1/a$, while those with $a > a(T_b)$ will contribute only at the inclination angle $\vartheta = 1/a(T_b)$. Combining these two contributions and employing the small angle approximation for sin ϑ we find

$$d\mathcal{N}(T_b) = \frac{1}{6a(T_b)} \frac{dT_b}{T_b} \times \left(\mathcal{N}(a[T_b]) + \frac{2}{a(T_b)} \int_{a(T_b)}^{\infty} \mathcal{N}(a) da \right) . \tag{5.12}$$

This result can be used to deduce the function $\mathcal{N}(a)$ from the observed distribution of brightness temperatures in a given source. As an example, consider a power-law distribution of aspect ratios, $\mathcal{N}(a) \propto a^{-p}$ ($p > 1$ to ensure convergence.) The corresponding distribution of brightness temperatures is also a power law, $\mathcal{N}(T_b) \propto T_b^{-(4+p)/3}$.

The coherence properties of the strong maser features in star-forming regions appear to be determined by chance order in a chaotic velocity field. These features appear to be individual structures defined by line-of-sight velocity coherence in an otherwise turbulent medium. In all likelihood, the structure of a single maser spot resembles more closely a filament rather than a sphere. As we have shown above, for either geometry the observed radiation emanates from a region that is shaped like a tube. But in the case of a filamentary maser this is the entire coherent region while in a sphere it is only part of a much larger volume whose properties are assumed identical to those of the observed emission tube. *The filamentary geometry provides the minimal realization of the velocity coherence dictated by observations*, and this makes it the most likely configuration in sources that display large velocity dispersion. The velocity gradients for certain directions will be, by chance, somewhat smaller than for others. The better velocity coherence introduces a preferred local axis leading to stronger radiation along it, which then increases the asymmetry and so on, resulting in an elongated structure.

Perhaps the most decisive arguments against the spherical geometry come from interferometric studies. Genzel et al. (1981) report that the observed sizes of individual maser spots in W51M are roughly constant across the profile; similar results were obtained for a number of maser sources by Walker and Moran (1990). Such behavior is expected only when the filamentary condition is obeyed. In addition, as shown in Paper II, the apparent radius of a typical astronomical maser would be only ~3% of its actual radius if it were shaped like a sphere. However, high-resolution mapping shows that the separation between maser spots is comparable to the diameters of individual features. Regions with dimension ~100 times the diameter of a single spot typically contain many features with different velocities. It is therefore highly unlikely that astronomical masers resemble homogeneous spheres, and this geometry is mostly only of theoretical interest. In all likelihood, strong features in astronomical maser sources are the result of filamentary geometry.

VI. SUMMARY

This section is a summary of the results with most direct relevance to observations. The pertinent equations are gathered together and the second-order corrections are displayed wherever applicable to provide a handy reference. The original equation numbers are maintained for easy tracking to their location in the manuscript. When the equations are modified, either because of second-order corrections or to provide a form that is easier to apply, a prime is added to the equation number.

When the length of a filamentary maser increases, its flux varies linearly according to

$$F_\nu(l) = 4\pi J_\nu(l) = 0.84 \times (7/12) \times 4\pi J_s \kappa_{0\nu} \ell \tag{3.11'}$$

while the solid angle of the radiation beam becomes narrower,

$$\Omega_\nu/4\pi = \omega_1(\Omega_0/4\pi) = 1/(11a^2) ; \tag{3.26}$$

the corresponding relation for the angular size of the beam pattern is

$$\vartheta_\nu = \omega_1^{1/2}\vartheta_0 = 0.60/a . \tag{3.26'}$$

The linear increase of the flux and quadratic increase of the beaming factor $4\pi/\Omega_\nu$ combine to produce brightness temperature variation with the third power of length according to

$$kT_b = 0.84\left(\frac{77}{24}\right) \frac{\lambda^2 h\nu}{4\pi} \Phi_{m\nu} R a^3 \tag{3.28'}$$

for observations along the axis. As an example, our model for H_2O masers in star-forming regions produces

$$T_b = 0.9\ 10^{12}(a/10)^3\ \mathrm{K} \tag{4.13}$$

for typical parameters. Other consequences of the beaming are (1) the isotropic luminosity overestimates the maser actual luminosity,

$$L_{\nu,\mathrm{iso}} = 0.84(77/24)a^2 L_\nu , \tag{5.5'}$$

and (2) the filaments appear smaller when viewed off-axis, the observed solid angle decreasing with an increase in observation angle ϑ according to

$$\Omega_{\mathrm{obs}} = 4R^2 \cos\vartheta/D^2 . \tag{5.8}$$

The variation of brightness temperature with length and viewing angle when all other properties are fixed is given by

$$T_b(a, \vartheta) \simeq T_0 a^3 \times \begin{cases} 1 & \vartheta \leq 1/a \\ 1/(a\vartheta)^3 & \vartheta \geq 1/a . \end{cases} \tag{5.10}$$

From this, the distribution of brightness temperatures observed for a filament ensemble can be calculated and the result is listed in equation (5.12). A power-law distribution of aspect ratios, $\mathcal{N}(a) \propto a^{-p}$, produces a power-law distribution of brightness temperatures, $\mathcal{N}(T_b) \propto T_b^{-(4+p)/3}$.

The effect of external radiation on the maser emission can be described by the parameter χ, the enhancement of intensity due to the external radiation (eq. [4.2]). The general result for the enhancement factor of a filamentary maser is

$$\chi = 1 + \frac{28}{11} \frac{T_e/T_{x0}}{\kappa_{0\nu}\ell} \left[1 + \frac{7}{16} \frac{T_e/T_{x0}}{\kappa_{0\nu}\ell} \left(\frac{\vartheta_e}{\vartheta_0} \right)^2 \right]^{-1} , \tag{4.6'}$$

where ϑ_e is the angle subtended at the maser by the external source, T_e is its brightness temperature and T_{x0} is the unsatu-

rated maser excitation temperature. This general expression can be used to derive the enhancement factor when the background source is itself a maser, as in the case of two interacting filaments (eq. [4.11]) for example.

This work was supported in part by NSF through grants AST-8615177 and AST-8716936, and NASA through grant RTOP 188-44-53 and a theory grant which supports the Center for Star Formation Studies.

APPENDIX A

EXACT EQUATION FOR THE BEAMING ANGLE

The solution presented in § III was the first-order solution, derived under the assumption of a constant $\omega(z)$, the ratio of the beaming angle $\Omega_\nu(z)$ to the cap solid angle (eq. [3.3]). In this Appendix we develop the exact integral equation that defines this unknown dimensionless function.

It is convenient to denote locations on the axis with the dimensionless coordinate

$$y = z/\ell \ . \tag{A1}$$

The cap's solid angle at y is then $4\Omega_0/(1 + y)^2$ and the function ω is defined from

$$\Omega_\nu(y) = \omega(y)\frac{4\Omega_0}{(1 + y)^2} \ . \tag{A2}$$

The solution of the equation of radiative transfer (3.5) for the dominant rays of a saturated filament is then

$$J_\nu(y) = J_s \kappa_{0\nu} \ell j(y) \ , \tag{A3}$$

where

$$j(y) = \frac{\omega(y)}{(1 + y)^2}\int_0^y \frac{(1 + y')^2}{\omega(y')}\, dy'$$

and where we assume, as we did throughout, that $z_{s\nu} \ll \ell$ and that J_s can be neglected in comparison with J_ν, since our primary interest is in $z \gg z_{s\nu}(y \gg 0)$. From this result it follows that

$$\alpha = J_\nu(\ell)/(J_s \kappa_{0\nu} \ell) = j(1) \ , \tag{A4}$$

where α is the structure constant defined in Paper II (see eq. [II.3.9]). Note that $\omega(y) =$ constant generates the first-order profile

$$j_1(y) = \frac{1}{3(1 + y)^2}(y^3 + 3y^2 + 3y) \ , \tag{A5}$$

which properly reproduces equation (3.9).

With equation (A3) for $J_\nu(y)$, it is a simple matter to solve for the intensity of the subordinate stream and obtain the equivalent of equation (3.13):

$$I_{\nu<}(z_{s\nu}, z_i) = S_0(\kappa_{0\nu}\ell)^2 \Psi(\zeta) \ , \tag{A6}$$

where

$$\Psi(\zeta) = \int_0^\zeta dy \omega(y) \int_0^y \frac{(1 + y')^2}{\omega(y')}\, dy' \ . \tag{A7}$$

This then provides the radiation angular distribution profile

$$\Theta(\zeta) = \Psi(\zeta)/\Psi(1) \ . \tag{A8}$$

Note again that the first-order profile obtained from $\omega(y) =$ constant is

$$\Psi_1(\zeta) = \tfrac{1}{12}(\zeta^4 + 4\zeta^3 + 6\zeta^2) \ , \tag{A9}$$

in agreement with the result of equation (3.19).

Since the solution is now fully determined, even if in implicit form, the angle-averaged intensity J_ν can be calculated from its defining relation $J_\nu = \int I_\nu\, d\Omega/4\pi$. The equation determining the unknown function $\omega(y)$ is obtained from the self-consistency of the derived result and the beaming relation (eq. [3.2]) assumed at the outset. As in § III*a*, the integration is divided to its cap and side contributions so that

$$J_\nu(y) = J_{\nu,\mathrm{cap}}(y) + J_{\nu,\mathrm{side}}(y) \ . \tag{A10}$$

The left-hand side is obtained from the beaming relation (eqs. [3.2] and [A2]), while the cap and side contributions are given in equations (3.21) and (3.22), respectively, with proper account for the different location; in particular, the contribution of the sidewall

can be brought to the form

$$J_{\nu,\mathrm{side}} = 2\vartheta_0^2 I_\nu(y, 1) \int_0^1 \Theta(\zeta)(y + \zeta)^{-3} d\zeta \tag{A11}$$

(see eq. [3.22]). Equation (A10) therefore becomes

$$\omega(y) = 1 + 2(1 + y)^2 \int_0^1 \frac{\Theta(\zeta) d\zeta}{(y + \zeta)^3} , \tag{A12}$$

which is the sought-after result. When $\Theta(\zeta)$ is inserted from equations (A7) and (A8), this becomes an inhomogeneous integral equation for the unknown function $\omega(y)$. Its solution fully defines the function $\omega(y)$, both scale and functional form, and provides the complete solution of the filamentary maser problem. This equation can be solved with an iterative technique: the function ω_n derived in the nth step is inserted in the right-hand side, thus producing the next solution ω_{n+1} on the left-hand side, and so on. The solution presented in § III was derived from the initial guess $\omega_1(y) = \omega_1$, a constant. The corresponding angular distribution Θ_1 is then the one listed in equation (3.19), and the next order solution ω_2 can be obtained after a straightforward, if somewhat laborious integration. The result is

$$\omega_2(y) = (2/11)[1 + 10y + 3y^2 - 6y^3 + 6(1 - y^2)^2 \ln(1 - 1/y)] . \tag{A13}$$

Note that $\omega_2(1) = 16/11$, thus the beaming angle of the emanating radiation used throughout the paper is correct to second order. The logarithmic divergence at $y \to 0$ ($z \to 0$) is of no concern because the discussion is confined to $z \gg z_{sv}$. A remarkably accurate representation of this function over the entire interval [0, 1] is provided by the simple expression

$$\omega_2(y) = (16/11) y^{-0.285} . \tag{A14}$$

Therefore, although the function ω is not constant, its variation in second order is $(\ell/z)^{0.285}$, which is reasonably slow.

Since the function ω_2 is known, the rest of the second-order solution can be easily worked out. We present the results for an arbitrary power law, $\omega_2 \propto y^{-p}$. The second-order variation of the angle-averaged intensity is then

$$j_2(y) = \frac{1}{3(1 + y)^2} \left(\frac{y^3}{1 + p/3} + \frac{3y^2}{1 + p/2} + \frac{3y}{1 + p} \right) ; \tag{A15}$$

note that the first-order solution is reproduced with $p = 0$ (see eq. [A5]). The parameter α that characterizes the emergent intensity (eq. [A4]) can now be obtained, and with $p = 0.285$, the second-order result is

$$\alpha_2 = 0.84\alpha_1 . \tag{A16}$$

Thus the first-order $\alpha_1 = 7/12$ is reduced by 16%, which can be considered the overall accuracy of the first-order solution. The variation of α_n in successive iterations provides a particularly suitable convergence test, because α involves an integral over the entire maser. The second-order angular distribution can be calculated similarly, and the result is

$$\Psi_2(\zeta) = \frac{1}{12} \left(\frac{\zeta^4}{1 + p/3} + \frac{4\zeta^3}{1 + p/2} + \frac{6\zeta^2}{1 + p} \right) ; \tag{A17}$$

again, the first-order distribution is recovered with $p = 0$ (see eq. [A9]). This completes the second-order solution of a single filament.

The corrections to the solution in the presence of external radiation can be worked out in a similar manner. The parameter $\mathscr{R}_e$ (eq. [4.5]) involves the beaming angle at core entrance where most of our approximations are least valid, so its usage is somewhat problematic in second order. This problem is avoided in the two limits where a direct solution is available. When the external radiation does not affect the maser structure ($\mathscr{R}_e \ll 1$), the enhancement factor χ is determined by the ratio of intensities at core entry in the unperturbed solution. It is easy to show that the general form of equation (4.4) for these intensities is

$$I_{\mathrm{ex}} = 4j(1) I_e \kappa_{0\nu} \ell , \qquad I_{\mathrm{in}} = \Psi(1) S_0 (\kappa_{0\nu} \ell)^2 , \tag{A18}$$

and their ratio, the enhancement factor, is thus

$$\chi = 1 + \frac{4j(1)}{\Psi(1)} \frac{\gamma_e}{\kappa_{0\nu} \ell} \tag{A19}$$

(see eq. [4.7]). It is easy to verify that the numerical coefficient 28/11 is recovered from this result with the first-order functions. Equation (A16) provides the second-order correction to $j(1)$, and from equation (A17) and $p = 0.285$,

$$\Psi_2(1) = 0.83 \times \Psi_1(1) . \tag{A20}$$

Thus the ratio $j(1)/\Psi(1)$ is essentially unchanged in second order and so χ is the same.

The other limit, $\mathscr{R}_e \gg 1$, corresponds to the situation where the maser structure is controlled by the external radiation. The general expression for χ is then

$$\chi = 1 + \frac{2\omega(1)}{j(1)} \left(\frac{\vartheta_0}{\vartheta_e} \right)^2 . \tag{A21}$$

The first-order coefficients reproduce equation (4.8) up to factor 6/7, as mentioned. The value of $\omega(1)$ is unchanged, while the second-order correction to $j(1)$ modifies this factor to 1.02, improving the adequacy of the coefficient 64/11 of equation (4.8). The expressions for χ derived in § IV therefore hold in second order.

APPENDIX B

THE RADIATIVE FLUX VECTOR

The component along the ith direction of the radiative flux vector $\boldsymbol{F}_\nu(z, r)$ is obtained from

$$F_{\nu i} = \int I_\nu(\boldsymbol{l})\boldsymbol{l} \cdot \boldsymbol{e}_i \, d\Omega \, , \tag{B1}$$

where $\boldsymbol{e}_i$ is the appropriate coordinate unit vector and $\boldsymbol{l}$ is the unit vector along the ray (Fig. 4). Consider the contribution of cap rays. The filamentary condition ensures that I_ν can be considered independent of $\boldsymbol{l}$. For an arbitrary point P at location (z, r), a coordinate set is chosen with its origin at the point $A(r, z = -\ell)$ and the x-axis along AO (Fig. 4). The components of the unit vector $\boldsymbol{l}$ are

$$\boldsymbol{l} = (-\sin \vartheta' \cos \phi, \; -\sin \vartheta' \sin \phi, \cos \vartheta') \tag{B2}$$

and the other relevant unit vectors are $\boldsymbol{e}_r = (-1, 0, 0)$ and $\boldsymbol{e}_z = (0, 0, 1)$. It is convenient to introduce the angle $\vartheta = R/l = R/(\ell + z)$. The solid angle element is $d\Omega = \sin \vartheta' \, d\vartheta' \, d\phi$ and for each ϕ, the ϑ'-variation corresponds to the tip of the ray moving along the appropriate AB segment. From the figure it is evident that

$$AB = (R^2 - r^2 \sin^2 \phi)^{1/2} + r \cos \phi \tag{B3}$$

and ϑ' varies in the interval $[0, \vartheta \times AB/R]$. It is convenient to transform all ϕ-integrations to the quadrant $[0, \pi/2]$. This can be accomplished with the introduction of two appropriate upper bounds for the ϑ' integrations

$$\vartheta^{\pm} = \vartheta[(1 - (r/R)^2 \sin^2 \phi)^{1/2} \pm (r/R) \cos \phi] \, . \tag{B4}$$

The z-component of $\boldsymbol{F}_\nu$ is then

$$F_{\nu z, \mathrm{cap}} = 2I_\nu \int_0^{\pi/2} d\phi \left(\int_0^{\vartheta^+} \vartheta' d\vartheta' + \int_0^{\vartheta^-} \vartheta' \, d\vartheta' \right) , \tag{B5}$$

where the small angle approximation was assumed for ϑ'. Straightforward expansion produces

$$F_{\nu z, \mathrm{cap}} = 2I_\nu \vartheta^2 \int_0^{\pi/2} d\phi [1 + (r/R)^2(\cos^2 \phi - \sin^2 \phi)] \, . \tag{B6}$$

The terms multiplying $(r/R)^2$ integrate to zero, and the result is

$$F_{\nu z, \mathrm{cap}}(z, r) = \pi \vartheta^2 I_\nu(z) \, , \tag{B7}$$

the standard beaming relation (note, in particular, that $F_{\nu z}$ is independent of r). Therefore, the cap contributions to $F_{\nu z}$ and J_ν are related by the standard beaming expression

$$F_{\nu z, \mathrm{cap}} = 4\pi J_{\nu, \mathrm{cap}} \, . \tag{B8}$$

The r-component of $\boldsymbol{F}_\nu$ is obtained from

$$F_{\nu r, \mathrm{cap}} = 2I_\nu \int_0^{\pi/2} d\phi \cos \phi \left(\int_0^{\vartheta^+} \vartheta'^2 \, d\vartheta' - \int_0^{\vartheta^-} \vartheta'^2 \, d\vartheta' \right) . \tag{B9}$$

The two ϑ'-integrals enter in a difference because the r-projection of $\boldsymbol{l}$ has opposite signs in the two quadrants of ϕ. As before, straightforward ϑ'-integration produces

$$F_{\nu r, \mathrm{cap}} = 4/3 I_\nu \vartheta^3 (r/R) \int_0^{\pi/2} d\phi [3 \cos^2 \phi + (r/R)^2(4 \cos^4 \phi - 3 \cos^2 \phi)]; \tag{B10}$$

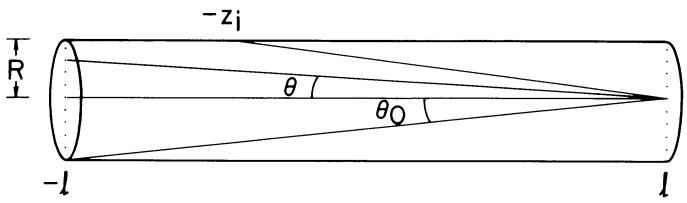

FIG. 4.—Calculation of the radiative flux vector $\boldsymbol{F}_\nu$

note that $\vartheta r/R = r/l$. Again, the terms multiplying $(r/R)^2$ integrate to zero and the final result is

$$F_{vr,\mathrm{cap}} = F_{vz,\mathrm{cap}} \frac{r}{\ell + z} . \tag{B11}$$

The radial component F_{vr} increases in proportion to r, the distance from the axis (from symmetry, F_{vr} obviously vanishes on the axis). The result $F_r : F_z = r : l$ implies that the flux vector is parallel to the line connecting the point with the center of the far cap, which is easy to understand: for every area element on the cap there is an equivalent element located diametrically opposite; the resultant contribution of the two elements to the flux vector is aligned with the *PO* axis.

These calculations provide the cap contribution to the flux at an arbitrary point. It is straightforward to show that the sidewall contribution maintains the relation of equation (B8) between F_{vz} and J_ν, and thus

$$F_{vz}(z, r) = F_\nu(z) , \tag{B12}$$

where $F_\nu(z)$ is given in equation (3.10). On the other hand, the relation of equation (B11) is only approximately obeyed by the sidewall contribution to F_{vr}. However, the deviation from this relation is not large—it is similar to the deviation of $\omega(z)$ from constancy along the filament. Since this difference affects only the contribution of the sidewall, which is smaller than that of the cap, it can be neglected at the level of accuracy of the first-order solution. Therefore, at the first order, the relation of equation (B11) applies to the overall components of the flux vector, F_{vr} and F_{vz}. This completes the definition of the radiative flux vector everywhere for the first iteration.

APPENDIX C

COMPARISON WITH OTHER GEOMETRIES

The first-order solution of the filamentary maser can be compared with both the linear and spherical masers. The resemblance with the linear maser is best illustrated by taking the $R \to 0$ limit of the filamentary maser solution. This limit cannot be taken directly because the intensity then diverges—as it should. The divergence occurs because the radiation is compressed into an infinitely narrow beaming cone. This is the same divergence that was mentioned in the discussion of the linear maser and is the reason why the functions $I_{\nu\pm}$ were introduced there (Paper I). The construction of an equivalent linear maser from a filamentary maser therefore requires that the coefficient in front of the singularity be identified. To do that we must first integrate over angles and then equate the corresponding emissivities in the filamentary and linear geometries through

$$\lim_{\Omega \to 0} \int I_\nu(z, 1) d\Omega = \int I_{\nu+}(z) \delta(\mu - 1) d\Omega . \tag{C1}$$

The intensity of the equivalent linear maser is thus

$$I_{\nu+}(z) = \lim_{\vartheta_\nu \to 0} \tfrac{1}{2} \langle \vartheta_\nu^2(z) \rangle I_\nu(z, 1) . \tag{C2}$$

In this expression, the beaming angle ϑ_ν was replaced by its average (as defined in Paper II) because the beaming angle of the filamentary maser varies with position while for a linear maser it is fixed. At the edge of the filament $\langle \vartheta_\nu^2(\ell) \rangle = (12/7)\omega_1 \vartheta_0^2$ and the intensity of the corresponding linear maser with half-length ℓ is

$$I_{\nu+}(\ell) = \lim_{R \to 0} \frac{24}{77} \left(\frac{R}{\ell} \right)^2 I_\nu(\ell, 1) . \tag{C3}$$

Inserting the filamentary maser first-order expression for I_ν (eq. [3.26]), the intensity obtained through this limit procedure is $I_{\nu+}(\ell) = 2 J_s \kappa_{0\nu} \ell$, in agreement with the result for the linear maser (Paper I). In addition, the various expressions obtained for the filamentary geometry are identical in form to those derived for the linear maser if the aspect ratio is considered a constant. The differences in the numerical coefficients of the two geometries reflect the radiation leakage through the filament sidewall, an effect that does not exist in the linear model.

The first-order filamentary maser solution also shares a lot of common properties with the spherical maser. In fact, with the formal substitution $r \to \ell + z$ the spherical maser solution can be carried over directly to the filamentary geometry. This correspondence can be understood from the discussion leading to equation (II.2.15), and its formal justification is provided by the calculations of the flux vector presented above (§ III; Appendix B). This substitution properly transforms the equation of radiative transfer from one geometry to the other since in the $z \geq z_{s\nu}$ saturated zone of a filamentary maser,

$$(\ell + z)^{-2} \frac{d}{dz} [(\ell + z)^2 J_\nu] = \kappa_{0\nu} J_s , \tag{C4}$$

similar to the spherical maser (see eq. [II.2.15]). Next, the expressions for the beaming angles are the same in both geometries (see eqs. [3.4] and [II.5.9]) and so the average beaming angle of the filamentary maser obeys

$$\langle \Omega(z) \rangle = \frac{3\Omega(z)}{1 + (\ell + z_{s\nu})/(\ell + z) + [(\ell + z_{s\nu})/(\ell + z)]^2} \tag{C5}$$

(see eq. [II.5.10]). Assuming $\ell \gg z_{sv}$ we again find $\alpha = \Omega(\ell)/\langle\Omega(\ell)\rangle = 7/12$. This result was also derived in Paper II from general flux considerations. It can be similarly obtained from the ratio of volume to surface area of a spherical shell with radii ℓ and 2ℓ, which can be understood from flux considerations and the correspondence with spherical geometry. Similarly, the optical depth between z_1 and z_2 in the saturated zone of a filamentary maser can be obtained from the corresponding expression for a spherical maser (eq. [II.5.16]):

$$\tau_v(z_1, z_2) = \ln \frac{(\ell + z_2)^3 - (\ell + z_{sv})^3\{1 - 3/[k_{0v}(\ell + z_{sv})]\}}{(\ell + z_1)^3 - (\ell + z_{sv})^3\{1 - 3/[k_{0v}(\ell + z_{sv})]\}} . \tag{C6}$$

In spite of the great similarity between the geometries, fundamental differences do exist. They stem from the difference in the location of the divergence center for the flux vectors. In a sphere this is the center, coinciding with the center of the core. In a filament, on the other hand, the flux divergence center is the center of the far cap, outside the core. Similarly, the base area A_0 which determines the beaming angle Ω_v (eq. [II.2.16]) is the visible area of the core of a sphere while in a filament it is the cap area of the far end. This causes the range of variation of the appropriate radii to be different. In the saturated shell of a spherical maser the radius varies from r_{sv} to R and the ratio of maximum to minimum radii can be almost arbitrarily high (the upper bound to this ratio is only met when the core finally saturates.) In contrast, the corresponding ratio in the filamentary maser is $2\ell/(\ell + z_{sv}) \lesssim 2$, which becomes constant, irrespective of the maser length once $\ell \gg z_{sv}$. The "equivalent radius" $\ell + z$ of a filamentary maser varies by only a factor of 2, independent of the actual source dimensions.

REFERENCES

Abraham, Z. et al. 1981, A&A, 100, L10
Burke, B. F., et al. 1973, Izv. Vyssh. Uchebn. Zaved., Radiofiz. 16, 799
Deguchi, S. and Watson, W. D. 1989, ApJ, 340, L17
Elitzur, M. 1990*a*, ApJ, 363, in press (Paper I)
———. 1990*b*, ApJ, 363, in press (Paper II)
Elitzur, M., Hollenbach, D. J., and McKee, C. F. 1989, ApJ, 346, 983 (EHM)
Elitzur, M., Hollenbach, D. J., and McKee, C. F. 1990, in preparation
Garay, G., Moran, J. M., and Haschick, A. D. 1989, ApJ, 338, 244
Genzel, R. 1986, in *Masers, Molecules, and Mass Outflows in Star Forming Regions*, ed. A. D. Haschick (Haystack Observatory), p. 233
Genzel, R. et al. 1981, ApJ, 247, 1039
Goldreich, P., and Keeley, D. A. 1972, ApJ, 174, 517
Matveenko, L. I. 1986, Soviet Astr. 30, 589
Walker, R. C., and Moran, J. M. 1990, private communication
Western, L. R. 1987, ApJ, 317, 858